Wind-Driven Circulation in a Shelf Valley. Part I: Mechanism of the Asymmetrical Response to Along-Shelf Winds in Opposite Directions

WEIFENG (GORDON) ZHANG

Applied Ocean Physics and Engineering Department,
Woods Hole Oceanographic Institution, Woods Hole, Massachusetts

STEVEN J. LENTZ

Physical Oceanography Department, Woods Hole Oceanographic Institution, Woods Hole, Massachusetts

ABSTRACT

Motivated by observations in Hudson shelf valley showing stronger onshore than offshore flows, this study investigates wind-driven flows in idealized shallow shelf valleys. This first part of a two-part sequence focuses on the mechanism of the asymmetrical flow response in a valley to along-shelf winds of opposite directions. Model simulations show that (i) when the wind is in the opposite direction to coastal-trapped wave (CTW) phase propagation, the shelf flow turns onshore in the valley and generates strong up-valley transport and a standing meander on the upstream side (in the sense of CTW phase propagation) of the valley, and (ii) when the wind is in the same direction as CTW phase propagation, the flow forms a symmetric onshore detour pattern over the valley with negligible down-valley transport. Comparison of the modeled upstream meanders in the first scenario with CTW characteristics confirms that the up-valley flow results from CTWs being arrested by the wind-driven shelf flow establishing lee waves. The valley bathymetry generates an initial excessive onshore pressure gradient force that drives the up-valley flow and induces CTW lee waves that sustain the up-valley flow. When the wind-driven shelf flow aligns with CTW phase propagation, the initial disturbance generated in the valley propagates away, allowing the valley flow to adjust to roughly follow isobaths. Because of the similarity in the physical setup, this mechanism of arrested CTWs generating stronger onshore than offshore flow is expected to be applicable to the flow response in slope canyons to along-isobath background flows of opposite directions.

1. Introduction

Submarine valleys over continental shelves and canyons over continental slopes are common features on the ocean floor (Allen and Durrieu de Madron 2009; Harris and Whiteway 2011). Canyons and valleys provide important pathways for transporting heat, salt, sediment, nutrients, and biological organisms across continental shelves and slopes (e.g., Bosley et al. 2004; Connolly and Hickey 2014; Crockett et al. 2008; Harris et al. 2003; Hickey et al. 1986; Williams et al. 2006). Compared to slope canyons (also called shelfbreak canyons), shallower shelf valleys, such as the Hudson shelf valley (Lentz et al. 2014), Umuda valley (Crockett et al. 2008), Swatch of No Ground (Michels et al. 2003),

and the valley east of Changjiang River mouth (Liu and Gan 2015), are in regions of active sediment transport and biological processes and strongly influenced by surface forcing, for examples, winds and surface waves. Connecting nearshore and offshore regions, shelf valleys can contribute substantially to cross-shelf transport of salt, heat, nutrients, fish larvae, and coastal contaminants (e.g., Manning et al. 1994; Schiller et al. 2011; Zhang et al. 2009).

There have been relatively few studies of circulation in shallow shelf valleys. Lentz et al. (2014) used historical observations to describe the vertical structure of circulation in the Hudson shelf valley (HSV) and the connection between the valley flow and wind forcing. HSV is a distinct geomorphological feature that is 20–30 m deep, about 5 km wide, and over 100 km long, cutting across almost the entire Mid-Atlantic Bight shelf. It connects the Hudson estuary with the outershelf

---

Corresponding author: Weifeng (Gordon) Zhang, wzhang@whoi.edu

region and potentially serves as a major conduit for cross-shelf exchange. Lentz et al. (2014) found that the flow in HSV is highly correlated with the wind-driven, cross-shelf pressure gradient and that the mean current in the valley is onshore, in contrast to the primarily along-shelf flow on the surrounding shelf. There is also a strong asymmetrical response of the along-valley flow to winds in opposite directions. The up-valley flow under eastward winds is stronger than the down-valley flow under westward winds, a pattern consistent with flows in slope canyons that has been well described in the literature.

Numerous numerical modeling studies have portrayed a consistent picture of asymmetrical canyon flow response to ambient along-slope flows in opposite directions (e.g., Allen and Durrieu de Madron 2009; Kämpf 2006; Klinck 1996; She and Klinck 2000). (i) When the ambient flow is in the same direction as coastal-trapped wave (CTW) phase propagation, the along-slope flow tends to roughly follow isobaths as it traverses the canyon, and along-canyon (cross shelf) transports are relatively weak. (ii) When the ambient flow is in the opposite direction to CTW propagation, strong onshore upwelling flow occurs in the canyon. The onshore flow generally concentrates on the upstream canyon slope, inducing relatively strong onshore transport of the offshore subsurface water. (Throughout this study, upstream and downstream are defined in the sense of CTW phase propagation.) Observations have also shown strong up-canyon flows (Freeland and Denman 1982; Hickey 1997). Interestingly, the up-canyon flows in these previous studies are similar to the dispersive supercritical leap of topographic Rossby waves over a localized narrow shelf in a channel when the background channel flow opposes the propagation of topographic Rossby waves (Haynes et al. 1993; Johnson and Clarke 1999, 2001). Consistent with the asymmetrical response, numerical and laboratory experiments forced by oscillatory slope currents have shown net onshore flows in canyons (Boyer et al. 2004, 2006; Haidvogel 2005). Moreover, Yankovsky and Chapman (1997) found flow responses at a canyon to the opposite phases of passing low-frequency CTWs are also asymmetrical.

The fundamental mechanism responsible for the asymmetrical response of canyon or valley flow to opposite along-shelf flows remains unknown. Previous studies have argued that strong up-canyon flows when the ambient flow opposes CTW propagation result from the excessive onshore pressure gradient caused by the canyon bathymetry suppressing the cross-canyon flow, reducing the offshore Coriolis force and breaking the cross-shelf geostrophic balance (Freeland and Denman 1982; Klinck 1989). However, this mechanism does not explain the absence of strong cross-shelf flow when the along-shelf flow is in the direction of CTW propagation. Yankovsky and Chapman (1997) considered the asymmetrical canyon flow response to the passing CTWs as a nonlinear scattering effect of the canyon bathymetry.

A few studies suggest the asymmetrical response to background along-shelf flow may be related to the influence of the irregular bathymetry on the propagation of shelf waves or Kelvin waves (Allen and Durrieu de Madron 2009; Killworth 1978). In particular, Allen and Durrieu de Madron (2009) proposed the idea that the asymmetry results from the background along-shelf flow arresting shelf waves in the upwelling scenario but not in the downwelling scenario. However, how this different interaction between the shelf flows and the shelf waves would lead to the asymmetrical flow response in the canyon is unclear.

The objectives of this study are to reveal the mechanism of the asymmetrical valley flow responses to along-shelf currents of opposite directions (Part I) and to understand the dynamical controls of the along-valley velocity (Zhang and Lentz 2017, manuscript submitted to *J. Phys. Oceanogr.*, hereinafter Part II). In this part, we show that the asymmetry in the valley flow is caused by the establishment of a CTW lee wave arrested at the valley by the along-shelf flow opposing the CTW propagation, a mechanism described by Martell and Allen (1979) and consistent with the hypothesis proposed by Allen and Durrieu de Madron (2009). When the along-shelf flow is in the same direction as CTW propagation there is no arresting of the CTW at the valley. Two types of numerical models are used here: a primitive equation model solving the full hydrostatic Navier–Stokes equations and a CTW model solving linear inviscid version of the equations.

2. Methods

a. Primitive equation model

The Regional Ocean Modeling System (ROMS; Shchepetkin and McWilliams 2008) is used in this study. It solves the Boussinesq hydrostatic equations of motion:

$$\frac{\partial u}{\partial t} + \mathbf{u} \cdot \nabla u - fv = -\frac{1}{\rho_0}\frac{\partial p}{\partial x} + \frac{\partial}{\partial z}\left(\kappa \frac{\partial u}{\partial z}\right), \qquad (1)$$

$$\frac{\partial v}{\partial t} + \mathbf{u} \cdot \nabla v + fu = -\frac{1}{\rho_0}\frac{\partial p}{\partial y} + \frac{\partial}{\partial z}\left(\kappa \frac{\partial v}{\partial z}\right), \qquad (2)$$

$$\nabla \cdot \mathbf{u} = 0, \qquad (3)$$

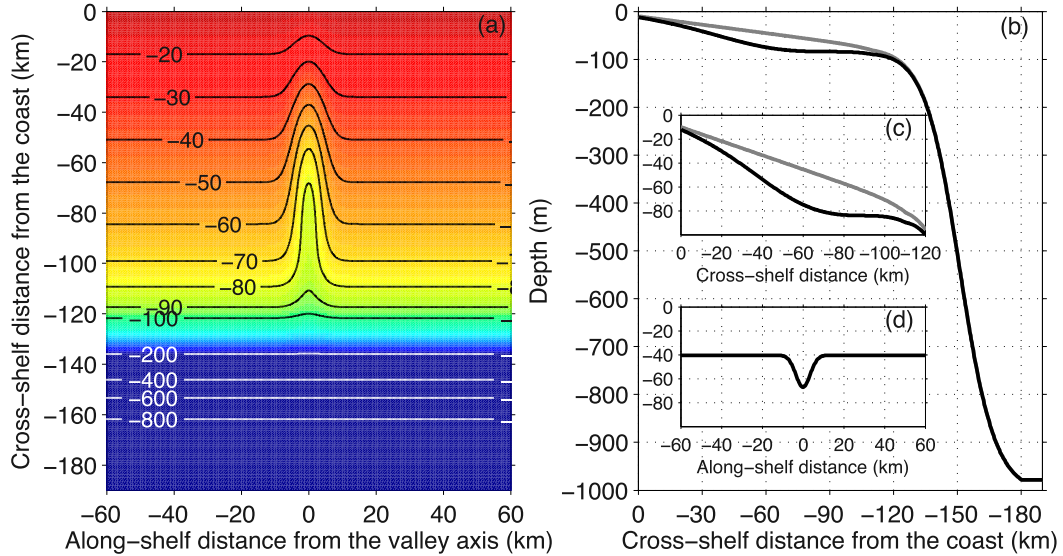$$\frac{\partial p}{\partial z} = -g\rho, \qquad (4)$$

FIG. 1. (a) Top and (b),(c) side view of the model bathymetry in the control scenario. (d) Along-shelf section of the bathymetry at $y = -50$ km. The gray lines in (b) and (c) are the ambient cross-shelf bathymetry outside of the valley, and the black lines are the cross-shelf bathymetry along the valley axis.

and

$$\frac{\partial \rho}{\partial t} + \nabla \cdot (\rho \mathbf{u}) = \frac{\partial}{\partial z}\left(\kappa_\theta \frac{\partial \rho}{\partial z}\right). \quad (5)$$

Here, positive x is defined as eastward along shelf (upstream), positive y is northward (onshore), and positive z is upward (Fig. 1). In (1)–(5), t is time; $\nabla = (\partial x, \partial y, \partial z)$ is the gradient vector; $\mathbf{u} = (u, v, w)$ with u, v, and w being velocity in the x, y, and z directions, respectively; f is the Coriolis parameter; p is hydrostatic pressure; g is gravitational acceleration; ρ_0 and ρ are the density constant and total density; and κ and κ_θ are vertical turbulence viscosity and diffusivity, respectively.

The model has a rectangular domain with edge lengths of 920 and 430 km in the x and y directions, respectively, and a coastal wall at the northern boundary. The idealized ambient shelf and slope bathymetry is

$$h_a = \max\left[0, \frac{h_f - h_c}{l_f}(l_f + y)\right] + h_p\left(\tanh\frac{y - y_p}{l_p} - 1\right) - h_f. \quad (6)$$

Here, the depth on the coast $h_c = 10$ m, the shelf depth scale $h_f = 75$ m, the shelf width scale $l_f = 110.3$ km, the y coordinate of the center of the slope $y_p = -151.3$ km, the slope width scale $l_p = 16.5$ km, and the slope vertical scale $h_p = 465$ m. This ambient bathymetry is along-shelf uniform. The water depth deepens offshore (southward) at a rate of about 0.6×10^{-3} on the shelf, transitions to a hyperbolic tangent shape on the slope with a maximum

depth of -1005 m. The 100-m isobath is located at $y = -121.7$ km. Values of the parameters are chosen to represent the shelf and slope bathymetry around HSV.

A Gaussian-shaped valley is added to the shelf as

$$h = h_a - H_c \exp\left[-\frac{(y - y_0)^2}{L_c^2} - \frac{(x - x_0)^2}{W_c^2}\right]. \quad (7)$$

Here, L_c, W_c and H_c are the valley length (cross-shelf direction), width (along-shelf direction), and depth scales, respectively, and (x_0, y_0) is the coordinate of the valley center, which is fixed at $x_0 = 0$, the along-shelf midpoint of the model domain, and $y_0 = -65.3$ km. Defining the valley edge to have a depth drop of 2% of its maximum value H_c, the total width of the valley is $W_T \approx 4W_c$.

The horizontal resolution of the model varies spatially. The grid spacing is 250 and 300 m in the along- and cross-shelf direction, respectively, in a central area of 160 km $\times$ 180 km that covers the valley. The grid spacing outside of that central area increases gradually outward reaching 3 km on the boundaries. There are 80 stretched vertical sigma layers with enhanced resolution near the surface and bottom.

The model has three open boundaries to the west, south, and east. The northern boundary is closed. Chapman (1985), Flather (1976), and zero-gradient conditions are used on the open boundaries for surface elevation, barotropic velocity, and baroclinic variables, respectively. A boundary sponge layer of 100 km wide with outward gradually enhanced horizontal viscosity is employed on all

three open boundaries to prevent wave reflection. The sponge layer is more than 300 km away from the valley and does not affect the valley flow. No explicit horizontal viscosity or diffusivity is used in the interior domain.

The model is forced on the surface by spatially uniform and temporally steady along-shelf winds (eastward or westward). Because the eastward wind stress drives upwelling flow both on the ambient shelf and in the valley, the simulations forced by eastward winds are referred to as upwelling simulations and simulations forced by westward winds are referred to as downwelling simulations. The initial buoyancy frequency N is horizontally uniform and varies in the vertical direction only across $z = -200\,\text{m}$, below which N is spatially uniform and equals $0.001\,\text{s}^{-1}$ in all simulations. The value of N in the surface 200 m is also uniform in all simulations. It is $0.01\,\text{s}^{-1}$ in the control simulations and varies among the sensitivity simulations (Table 1). All simulations start from zero velocity everywhere and are run for 10 days with quadratic bottom friction and no surface or bottom buoyancy flux. In the control cases, $f = 9.37 \times 10^{-5}\,\text{s}^{-1}$ (latitude 40°) everywhere; the surface wind stress $\tau_s = \pm 0.2\,\text{N}\,\text{m}^{-2}$, a typical value for the HSV region (Lentz et al. 2014); the quadratic bottom drag coefficient $C_d = 0.003$.

As this work is motivated by the observations in HSV, the sensitivity study here focuses on the part of the parameter space surrounding HSV and considers seven sensitivity parameters: τ_s, f, N, W_c, L_c, H_c, and C_d. Seven sets of upwelling and downwelling sensitivity simulations with varying parameter values are conducted. Within each set, the value of only one parameter is altered, and all other parameters are kept at their control values (Table 1). There are a total of 42 pairs of simulations described in this part of the study, including a pair with flat shelf bathymetry and a pair with a slip bottom ($C_d = 0$) and $\tau_s = \pm 0.1\,\text{N}\,\text{m}^{-2}$ (see below).

The variations of the sensitivity parameters are kept in ranges that give the valley Burger number S and Rossby number Ro generally in the same category as in the control scenario (Table 1). Here,

$$S = \frac{NH_c}{fW_c},\tag{8}$$

and

$$\text{Ro} = \frac{|U_s|}{fW_c},\tag{9}$$

with U_s being the cross-shelf and depth-averaged along-shelf velocity away from the valley. In the control cases, $U_s \approx 0.45\,\text{m}\,\text{s}^{-1}$, $S = 0.64$, and Ro = 0.94. Among the sensitivity simulations, S varies from 0 to 2 with most (36 out of the 42 pairs) being less than 1; Ro varies from

0.24 to 3.25, all being $O(1)$. The generally small to moderate S means that the width of the valleys considered in this study is the same order of magnitude as or greater than the valley internal radius NH_c/f. The $O(1)$ Ro means that momentum advection is important in the valley flows, and the valley width is the same order of magnitude as the momentum advection length scale $|U_s|/f$, which will be discussed in detail in Part II.

b. Coastal-trapped wave model

A model for Boussinesq, hydrostatic, linear inviscid CTWs (e.g., Brink 1990, 2006) along a straight coast is also used here. The governing equations are

$$\frac{\partial u}{\partial t} - fv = -\frac{1}{\rho_0}\frac{\partial p}{\partial x},\tag{10}$$

$$\frac{\partial v}{\partial t} + fu = -\frac{1}{\rho_0}\frac{\partial p}{\partial y},\tag{11}$$

$$0 = -\frac{\partial p}{\partial z} - g\rho',\tag{12}$$

$$\nabla \cdot \mathbf{u} = 0,\tag{13}$$

and

$$\frac{\partial \rho'}{\partial t} + w\frac{\partial \overline{\rho}}{\partial z} = 0.\tag{14}$$

Here, the density deviation ρ is separated into

$$\rho = \rho_0 + \overline{\rho}(z) + \rho'(x,y,z,t),\tag{15}$$

with $\overline{\rho} \gg |\rho'|$. Combining (10)–(14) gives the pressure-based vorticity equation

$$\left(f^2 + \frac{\partial^2}{\partial t^2}\right)\frac{\partial}{\partial z}\left(\frac{1}{N^2}\frac{\partial^2 p}{\partial z \partial t}\right) + \frac{\partial^3 p}{\partial x^2 \partial t} + \frac{\partial^3 p}{\partial y^2 \partial t} = 0.\tag{16}$$

The model looks for CTW solutions in the form of $p = P(y,z)\exp(i\omega t + ilx)$. Here, P is the modal structure that varies in cross-shelf and vertical directions; ω is the wave frequency; and l is the real positive alongshore wavenumber. For simplicity, bottom friction is neglected in the calculation. The boundary conditions of the model are the free-slip bottom condition

$$\frac{f^2 - \omega^2}{N^2}\frac{\partial P}{\partial z} = -\frac{dh}{dy}\left(\frac{fl}{\omega}P + \frac{\partial P}{\partial y}\right) \quad \text{at} \quad z = -h,\tag{17}$$

free-surface condition

$$g\frac{\partial P}{\partial z} - N^2 P = 0 \quad \text{at} \quad z = 0,\tag{18}$$

closed condition on the coastal boundary

TABLE 1. Model sensitivity parameters and corresponding nondimensional numbers.

Symbol	Sensitivity parameter	Unit	Sensitivity values[a]	$\text{Ro}^{[b]} = U_s/fW_c$	$S^{[c]} = NH_c/fW_c$
L_c	Valley length scale	km	20	0.94	0.64
			30	0.94	0.64
			40(*)	0.94	0.64
			50	0.94	0.64
			60	0.94	0.64
W_c	Valley width scale	km	2.5	1.88	1.28
			3.75	1.25	0.85
			5(*)	0.94	0.64
			7.5	0.63	0.42
			10	0.47	0.32
			15	0.31	0.22
			20	**0.24**	0.17
H_c	Valley depth scale	m	5	0.94	0.10
			15	0.94	0.32
			30(*)	0.94	0.64
			40	0.94	0.85
			50	0.94	1.07
C_d	Drag coefficient	10^{-3}	0.5	1.69	0.64
			1	1.33	0.64
			2	1.06	0.64
			3(*)	0.94	0.64
			4	0.87	0.64
			6	0.79	0.64
			10	0.70	0.64
f	Coriolis parameter	$10^{-5}\,\text{s}^{-1}$	3	**3.25**	**2.00**
			5	1.81	1.20
			7	1.27	0.85
			9.37(*)	0.94	0.64
			12	0.73	0.50
			15	0.57	0.40
N	Stratification	$10^{-2}\,\text{s}^{-1}$	0	0.95	**0**
			0.45	0.94	0.28
			0.71	0.94	0.46
			1(*)	0.94	0.64
			1.4	0.94	0.89
			1.7	0.95	1.09
			2.3	0.96	1.47
$|\tau_s|$	Wind stress	$\text{N}\,\text{m}^{-2}$	0.05	0.43	0.64
			0.1	0.64	0.64
			0.2(*)	0.94	0.64
			0.3	1.16	0.64
			0.4	1.34	0.64
			0.5	1.50	0.64
			0.6	1.64	0.64
			0.7	1.78	0.64
$|U_s|^{[d]}$	Along-shelf velocity	$\text{m}\,\text{s}^{-1}$	0.32	0.67	0.64
			0.36	0.77	0.64
			0.64	0.87	0.64
			0.45	0.97	0.64
			0.50	1.06	0.64
			0.54	1.16	0.64
			0.59	1.25	0.64
			0.63	1.34	0.64
			0.67	1.43	0.64
			0.72	1.53	0.64
			0.76	1.62	0.64
			0.80	1.71	0.64

[a] The control value of each parameter is indicated by the asterisk symbol.
[b] Defined based on the cross-shelf-averaged along-shelf velocity on the ambient shelf, U_s at the equilibrium state, except for the simulation of $C_d = 0$; the maximum and minimum values of the Rossby number are highlighted in bold.
[c] Defined based on the initial stratification in the top 200 m; the maximum and minimum values of the Burger number are highlighted in bold.
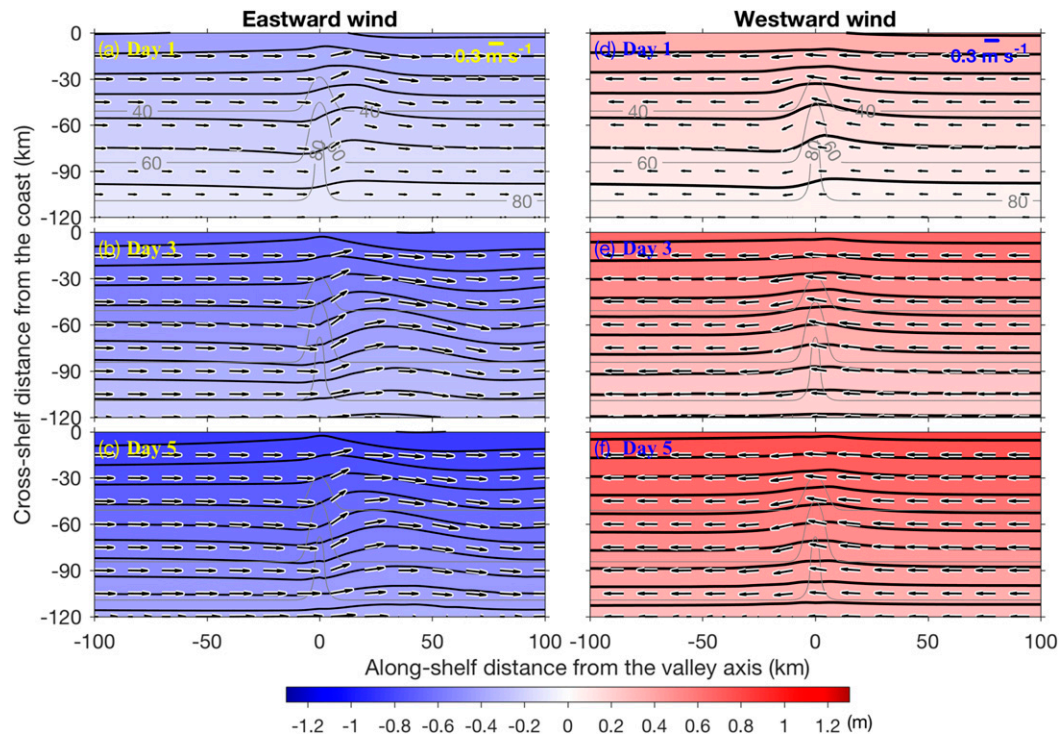[d] Obtained from the solutions of the slip-bottom simulations ($C_d = 0$) at different times.

FIG. 2. Plan views of modeled sea surface height (color and contours) and depth-averaged velocity (arrows) in the case of (left) eastward and (right) westward wind at days 1, 3, and 5. The gray lines in the background are isobath contours (m).

$$\omega \frac{\partial P}{\partial y} + flP = 0 \quad \text{at} \quad y = 0, \qquad (19)$$

and a zero-gradient condition on the offshore boundary

$$\frac{\partial P}{\partial y} = 0 \quad \text{as} \quad y \to -\infty, \qquad (20)$$

which ensures coastal trapping.

This CTW model solves (16)–(20) with the ambient bathymetry of (6) and the same f and N as the ROMS control simulations. The mean shelf flow is assumed to be zero. The vertical cross-shelf section is transformed to a stretched vertical coordinate system and discretized into 300 and 50 uniform grid intervals in the cross-shelf and vertical directions, respectively. The equations are solved numerically using resonance iteration (Wang and Mooers 1976) with a nominal accuracy of 0.1% for the absolute value of frequency. The results are (i) the CTW dispersion curves for different cross-shelf modes and (ii) the cross-shelf distributions of pressure, along-shelf velocity, and cross-shelf velocity associated with each mode.

3. General flow pattern

The basic pattern of the wind-driven flows resolved by the ROMS simulations is presented with an emphasis on the asymmetry in the wind-driven flow response in the valley. The flow on the shelf, far from the valley, is primarily along-shelf in the direction of the wind forcing and symmetrical with respect to the wind direction. After the initial adjustment, the speed of the cross-shelf- and depth-averaged along-shelf velocity in both cases $|U_s| \approx 0.45 \, \text{m s}^{-1}$. Upon encountering the valley, the circulation pattern is different under eastward versus westward winds.

a. Upwelling scenario under eastward wind

In the case of eastward wind (opposing CTW propagation; Figs. 2a–c), the shelf flow veers onshore at the valley with a positive (cyclonic) vorticity. It then turns back offshore with a negative (anticyclonic) vorticity after passing over the valley settling back at the original cross-shelf position. The onshore turn at the valley and the offshore turn to the east of the valley together form a meander pattern, which extends farther toward the east with time as the ambient flow accelerates. This meander pattern on the upstream side of the valley is consistent with the numerical model simulation of the circulation over a slope canyon (Kämpf 2012). At day 5 the circulation pattern is approximately in steady state, and the length of the meander in the ROMS simulation reaches 80 km. The flow to the west of the valley remains largely along isobath over the entire period.
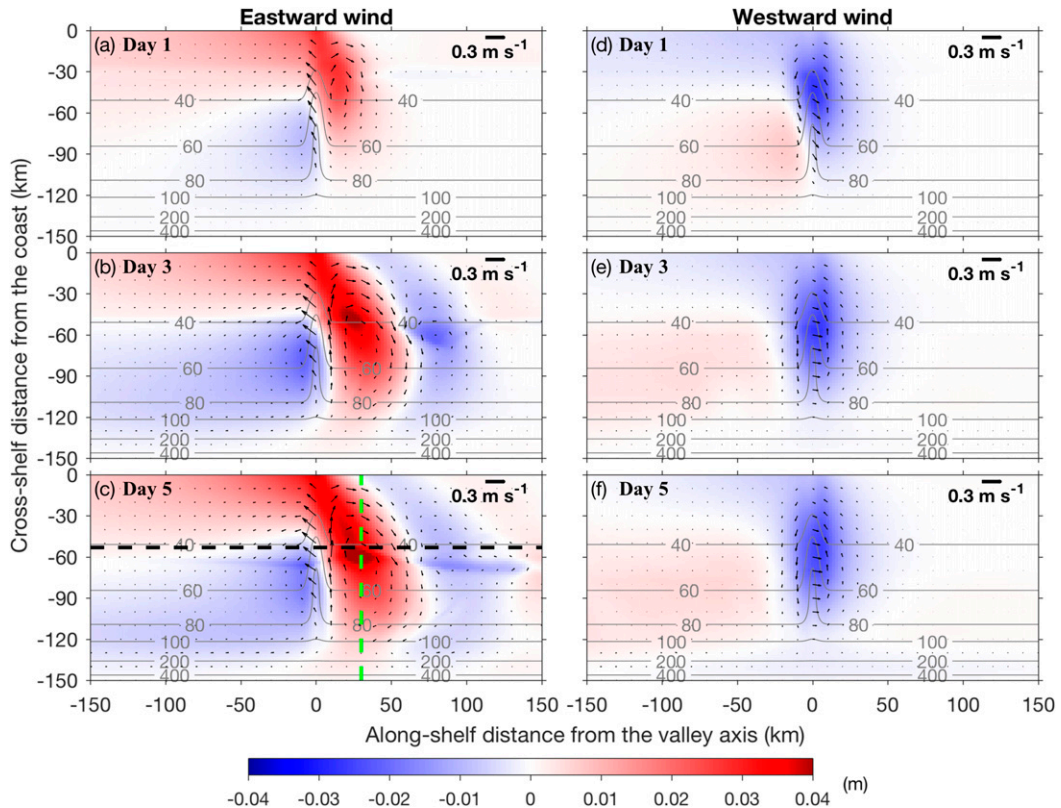
FIG. 3. Plan view of modeled SSH anomaly (color) and depth-averaged velocity anomaly (arrows) in the cases of (left) eastward and (right) westward wind at days 1, 3, and 5. The anomaly is defined as deviation from the conditions at 200 km to the west (east) of the valley in the case of eastward (westward) wind. The gray lines are isobath contours (m). The black and green dashed lines in (c) indicate the cross sections that data in Fig. 10a and Figs. 14e and 14f are extracted from, respectively. Note that the along- and cross-shelf extents of the figures here are greater than those in Fig. 2.

To separate the valley-induced flow from the background flow and investigate the valley influence, we computed the anomalies of sea surface height (SSH), η', and anomalies of the depth-averaged flow, $\mathbf{U}' = (U', V')$, everywhere with respect to those on the cross-shelf section 200 km to the west of the valley ($x = -200$ km) at each instant in time. The pattern of $\mathbf{U}'$ depicts a persistent up-valley flow anomaly sandwiched between cyclonic and anticyclonic recirculations to the west and east of the valley, respectively (Figs. 3a–c). Analysis of the momentum balance in Part II shows that the initial up-valley flow results from the bathymetrically induced excessive up-valley pressure gradient force, as the valley bathymetry breaks the geostrophic balance achieved on the ambient shelf, as previously argued by Klinck (1989) and Freeland and Denman (1982). The anticyclonic recirculation to the east of the valley is much stronger than the cyclonic recirculation to the west. The flow anomaly turns offshore to the east of the valley ($x \approx 50$ km and $t =$ days 3–5) following the strong anticyclonic recirculation

pattern with positive η'. The center of the anticyclonic pattern to the east of the valley migrates offshore and eastward over the first 3 days and remains stationary for the rest of the simulation. Starting from day 3, there is a weak cyclonic flow anomaly with negative η' developing to the east of the anticyclonic pattern ($x \approx 80$ km) and extending farther to the east over the next 2 days and then becoming stationary.

The vertical characteristics of the onshore flow in the valley differ dramatically from the wind-driven upwelling flow on the shelf. The flow on the cross-shelf section at $x = -200$ km is a typical wind-driven upwelling flow with the upwelling front located at $y = -50$ km (Figs. 4a,b). Farther offshore there are onshore and offshore flows in the bottom and surface Ekman layers, respectively. The cross section along the valley axis shows a strong bottom-intensified up-valley flow with a peak speed of $0.4 \, \mathrm{m \, s^{-1}}$ (Figs. 5a,b). The up-valley flow brings the offshore denser water shoreward in a well-mixed bottom layer of ~ 30 m thick and establishes
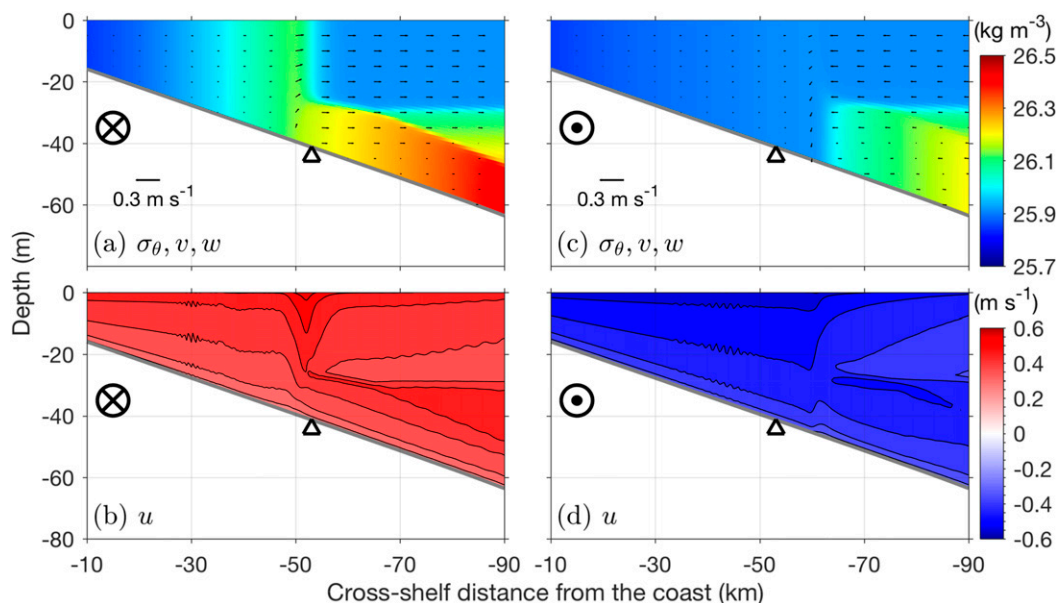
FIG. 4. Cross-shelf section of (top) density (color), cross-shelf and vertical velocities (arrows), and (bottom) along-shelf velocity on the ambient shelf ($x = -200$ km for the left and 200 km for the right) at day 3 in the case of (left) eastward and (right) westward wind.

strong stratification at the top of the bottom layer. The along-shelf (cross valley) flow on the valley axis weakens downward and reaches 0 near the bottom (Fig. 5b). The flow pattern on a midshelf alongshore section (Figs. 6a,b) shows the along-shelf flow dips into the valley, but the cross-valley flow is very weak below the valley rim. The up-valley flow occupies the entire water column over the valley and peaks on the eastern valley slope. The associate up-valley transport integrated over the whole water column and over the valley width W_T is $Q_v = 0.15$ Sv (1 Sv $\equiv 10^6$ m^3 s^{-1}).

The up-valley flow is also a persistent feature. The depth-averaged cross-shelf flow in the valley increases with the wind-driven along-shelf flow initially, reaches the peak of 0.22 m s^{-1} at day 1, and then remains at that level for the rest of the simulation (Fig. 7b). Away from the valley the vertically averaged cross-shelf flow remains negligible (Fig. 7a).

b. Downwelling scenario under westward wind

The flow pattern around the valley under westward wind (same direction at CTW propagation) differs dramatically from the flow pattern under eastward winds. Under westward wind, the westward flow veers shoreward approaching the valley and then veers seaward west of the valley axis and returns to its original cross-shelf position (Figs. 2d–f). The relative vorticity over the valley is positive. By day 3, the flow over the valley is roughly symmetrical with respect to the valley axis.

Anomalies η' and U', with respect to those at 200 km to the east of the valley ($x = 200$ km), show a cyclonic recirculation pattern centered over the valley with peak flows of 0.2 m s^{-1} (Figs. 3d–f), weaker than the anticyclonic recirculation under eastward wind.

A typical wind-driven downwelling flow with onshore (offshore) flow in the surface (bottom) Ekman layer is generated on the cross-shelf section at $x = 200$ km (Figs. 4c,d). Along the valley axis, a weak down-valley flow is generated with a peak speed of less than 0.1 m s^{-1} (Figs. 5c,d). The flow on the along-shelf section (Fig. 6c) shows the westward cross-valley flow reaching deep into the valley with a nearly uniform speed, differing from the eastward wind case. The along-valley flow reverses direction in the valley; there is an up-valley flow on the eastern valley slope and a down-valley flow on the western valley slope with the transition slightly to the east of the valley axis (Fig. 6d). The flow on the valley axis is down-valley and weak. The associated down-valley transport integrated over the entire valley cross section $Q_v = -0.023$ Sv is 7 times weaker than the up-valley transport under the same magnitude eastward wind. The difference in transport is because the up-valley flow under eastward winds is both stronger and over a broader region than the down-valley flow under westward winds. The spatial variation of the flow in the valley makes it hard to accurately estimate the along-valley transport under westward wind using a single-point velocity measurement; this is discussed in
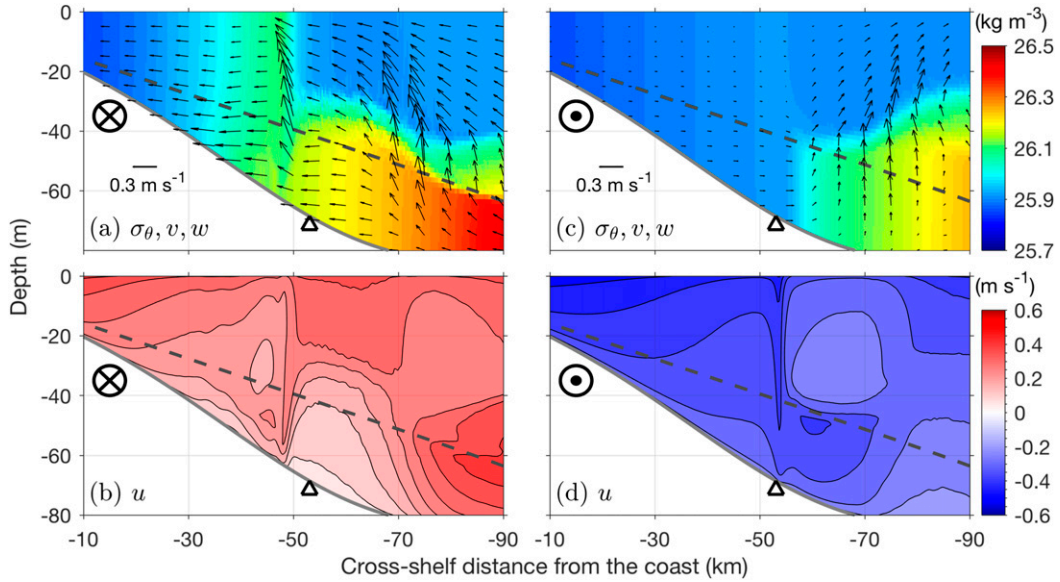
FIG. 5. As in Fig. 4, but along the valley axis. The dashed gray lines indicate the seafloor on the ambient shelf.

section 5. During westward wind the depth-averaged offshore flow on the valley axis varies over time (Fig. 7). It strengthens initially, reaching a peak of $-0.12 \, \mathrm{m \, s^{-1}}$ at about $t = 0.75$ day, and then weakens to $-0.03 \, \mathrm{m \, s^{-1}}$ at $t = 1.5$ day. For the rest of the simulation, the down-valley flow remains weak and steady.

This example emphasizes the dramatic contrast in the valley circulation in the upwelling and downwelling scenarios: the up-valley flow and transport under eastward wind is much stronger than the down-valley flow and transport under westward wind. This asymmetry in the responses of along-valley flow and transport to along-shelf winds of opposite directions applies to all the sensitivity simulations and thus persists over the range of Ro represented by the simulations (Fig. 8). Note that the along-valley flow and transport in both scenarios vary
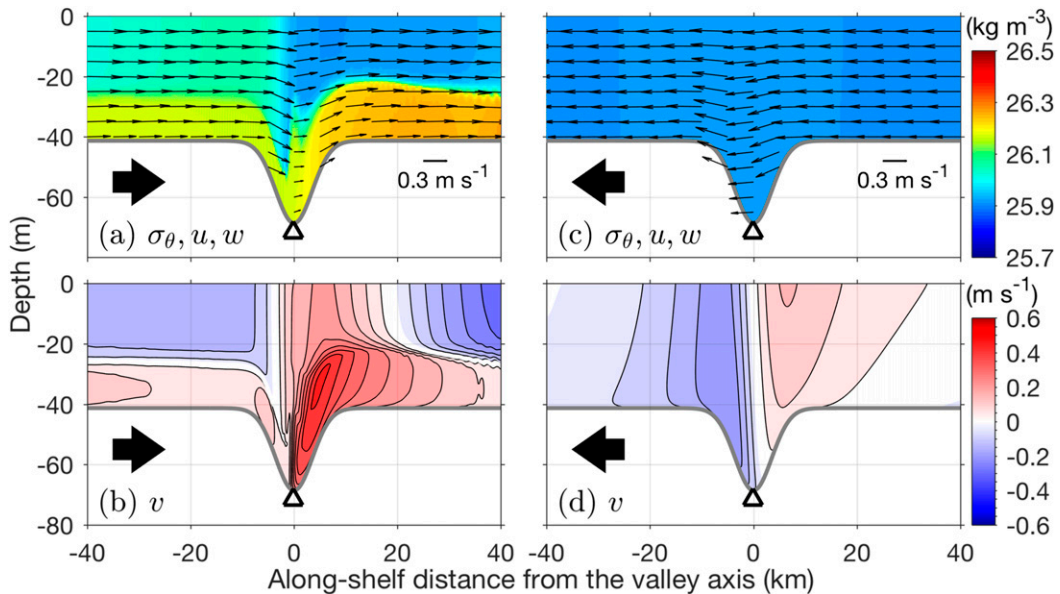
FIG. 6. Along-shelf section of (top) density (color), along-shelf and vertical velocities (arrows), and (bottom) cross-shelf velocity at $y = -52$ km at day 3 in the case of (left) eastward and (right) westward wind. The thick arrows indicate the wind direction.
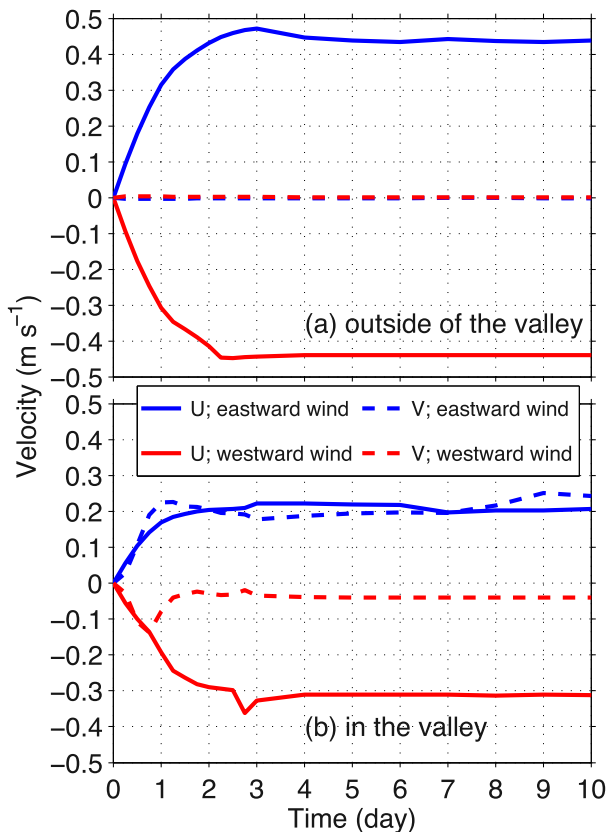
FIG. 7. Time series of depth-averaged velocity (a) outside of the valley ($x = -200$ km) and (b) on the valley axis ($x = 0$ km) at $y = -52$ km.

with Ro and the sensitivity parameters, which will be examined in detail in Part II. Another contrast between the scenarios is that the flow pattern under eastward wind is asymmetrical with respect to the valley axis with a persistent meander to the east of the valley, while the flow pattern under westward wind is symmetrical with respect to the valley axis. These contrasts are consistent with the asymmetrical responses of the valley flow to winds of opposite directions observed in the HSV (Lentz et al. 2014) and qualitatively similar to the different flow response in a slope canyon to along-slope current or wind in opposite directions, as described in section 1.

4. Connection to coastal-trapped waves

A potential explanation for the asymmetrical wind-driven valley flow is that the shelf flow under eastward wind arrests CTWs generated at the valley sustaining an onshore flow in the valley, while the shelf flow under westward wind allows CTWs to propagate away from the valley region. As pointed out by Martell and Allen (1979), a shelf flow over a valley or hump generates a

coastal-trapped lee wave when the shelf flow is in the opposite direction to CTW propagation. This lee-wave phenomenon is also captured by Narimousa and Maxworthy (1985) in a laboratory study. A coastal-trapped lee wave would not exist under westward wind because the westward shelf flow is in the direction of CTW propagation and hence cannot arrest a CTW. The persistent and stationary meanders to the east of the valley in the upwelling scenario resemble a lee wave. The following sections show that the upstream meanders are coastal-trapped lee waves.

a. Effect of sloping shelf

We first seek to confirm the role of CTWs in causing the different wind-driven valley flows. As the CTWs that can directly affect the valley flow require a sloping bottom (Kelvin waves are too fast to affect the valley flow; see below), we eliminate that type of CTWs in two new simulations by making the cross-shelf bathymetry flat at water depth $h_{af} = -50$ m. The model has no slope or deep sea but retains a Gaussian-shaped valley. The model bathymetry is

$$h = h_{af} - H_c \exp\left[-\frac{(x - x_0)^2}{W_c^2}\right]. \qquad (21)$$

The model boundary conditions are the same as those described in section 2a. The valley width and depth scales as well as other model parameters remain the same as in the control simulations.

The flow patterns resolved by these flat shelf simulations under eastward versus westward winds are mirror images to each other (Fig. 9). Under eastward wind, the flow at the valley turns onshore (Fig. 9). After passing through the valley, the flow turns back offshore. The flow under westward makes an offshore turn at the valley followed by a slight onshore turn back to along-isobath. This symmetry also exists on the along- and cross-shelf sections (not shown). The up-valley and down-valley flows under the respective eastward and westward winds mirror each other in both location and strength.

This difference between the control and flat-bottom simulations supports the idea of CTWs playing a role in forming the asymmetrical wind-driven valley flows. As the main asymmetry here is the westward propagation of CTWs ($f > 0$ and coast to the north), the interaction between the wind-driven shelf flow and CTW propagation is presumably the cause of the asymmetrical valley flows.

b. Upstream meander under eastward wind

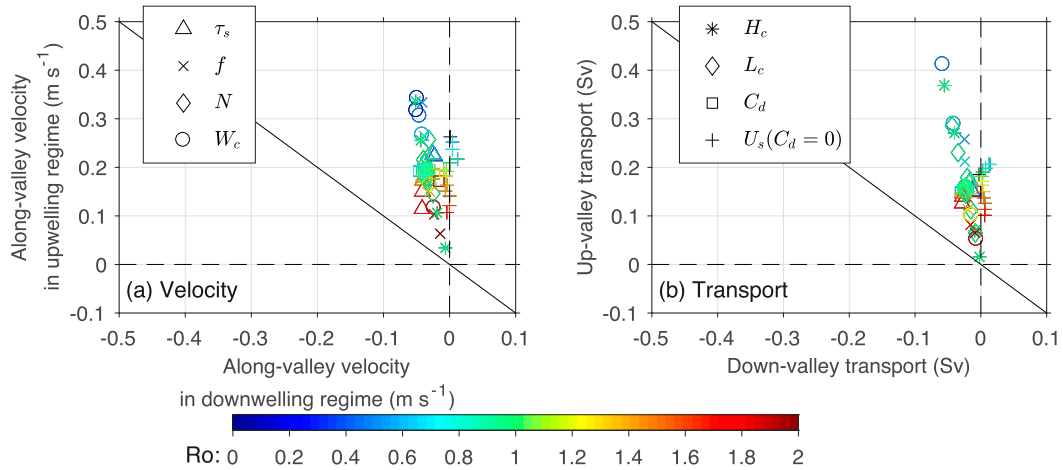To quantify the characteristics of the upstream meander in the upwelling control simulation, an along-shelf

FIG. 8. Comparison of the along-valley (a) velocity and (b) transport between the upwelling and downwelling simulations with the same parameter values. The along-valley velocity is obtained at $x = 0$ (valley axis) and $y = -52$ km, and the net along-valley transport is averaged over the cross-valley section at $y = -52$ km. Each type of symbol represents results from a sensitivity simulation series that varies one parameter corresponding to the legends, and the symbols are color-coded with Rossby number of the simulations. The solid lines represent the one-to-one correspondence.

slice of the SSH anomaly η' is taken on day 5 along $y = -52$ km, the center of the upstream anticyclonic flow anomaly. It shows an undulation of η' to the east of the valley with the maximum value of 0.04 m at $x = 20$ km, well upstream of the valley, and a minimum value of -0.008 m at $x = 80$ km (black line in Fig. 10a). The wavelength of the meander λ, computed as twice the distance between the maximum and minimum values, is 120 km.

In the upwelling control simulation the maximum η' and λ grow over the first 1.5 days and then remain constant for the rest of the simulation (Fig. 11a). At about day 1, a weakly negative η' signal appears to the west of the valley and propagates westward in the speed of about 5 m s^{-1} (gray dashed line in Fig. 11a). As time proceeds, alternating positive and negative η' peaks appear to the east with roughly the same wavelength. This eastward extension of the η' undulation is consistent with the gradual upstream propagation of the lee-wave front found by Martell and Allen (1979), and the speed of the extension generally matches the speed of the mean along-shelf flow U_s (thick black dashed line in Fig. 11a). In contrast, the time evolution of η' under westward wind shows westward propagation of a weakly positive η' signal in the first several days at a speed of about 5 m s^{-1} (gray dashed line in Fig. 11b) and then a gradual transition to a steady pattern that is roughly symmetric with respect to the valley axis. This temporal evolution of the anomaly signal is consistent with the notion that the initial disturbances excited by the flow over the bathymetric perturbation propagates away to

the west, allowing the flow to adjust to the valley bathymetry, reaching a symmetric detour pattern. The westward propagation of the initial disturbances will be discussed in section 5a.

To show the upstream meanders are coastal-trapped lee waves, we compare the characteristics of the meanders to results of the CTW model. To facilitate comparisons to the CTW model with no bottom friction (section 2b), two extra ROMS simulations were conducted with a slip bottom, that is, $C_d = 0$, and forced by uniform along-shelf winds in opposite directions. In the absence of bottom friction balancing the surface wind stress, the along-shelf velocity increases persistently with time and can reach unrealistic values quickly. Because the increasing shelf velocity provides an opportunity to examine the response of the valley flow to ambient shelf flow of different strength, a slowly increasing shelf flow is desired. The slip-bottom simulations are thus forced by wind stress of ±0.1 N m^{-2}, half of the wind stress used in the control simulations. Besides C_d and the wind stress, everything else in these slip-bottom simulations remains the same as in the control simulations.

The terms η' and $\mathbf{U}'$ in the slip-bottom simulations (Fig. 12) have qualitatively similar patterns as those in the control simulations (Fig. 3). In particular, the control and slip-bottom simulations of westward winds both have the negative η' and cyclonic flow anomaly sitting over the valley forming a symmetric pattern with respect to the valley axis. In the case of eastward wind, the up-valley flow anomaly and the anticyclonic anomaly
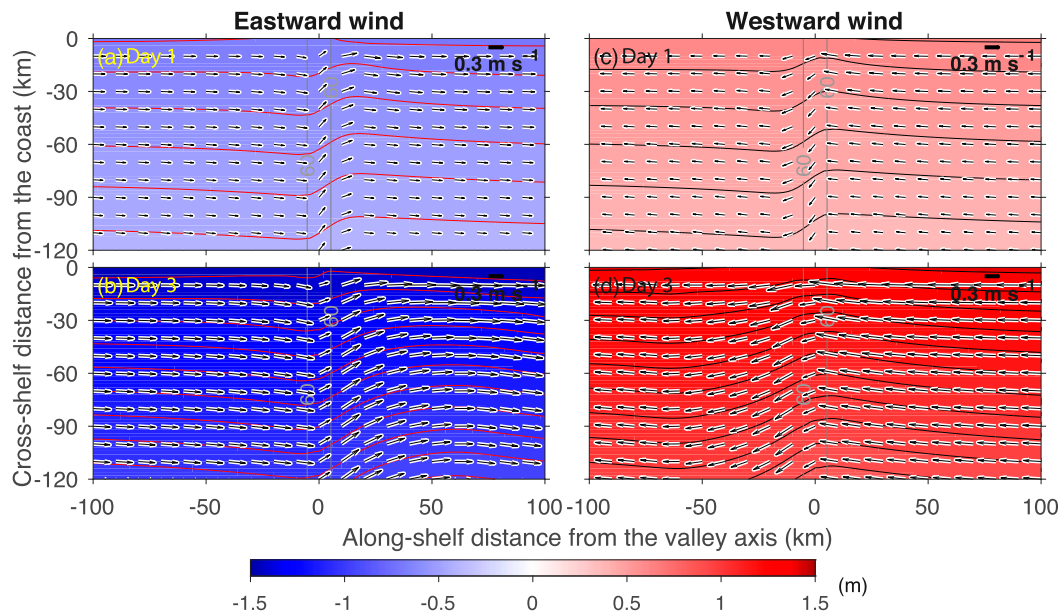
FIG. 9. Time series of modeled sea surface height (color) and depth-averaged velocity (arrows) in the case of (left) eastward and (right) westward wind with a flat shelf and a valley. The gray lines are isobath contours.

pattern to the east of the valley are preserved in the slip-bottom simulation (Figs. 12a–c). The center of the anticyclonic pattern also migrates offshore with time, as in the control simulation. One difference between the control and slip-bottom simulations of eastward wind is the strong negative η' and positive $\mathbf{U}'$ near the coast to the east of the valley in the former but not in the latter. Another difference is the faster upstream extension of the anticyclonic flow anomaly in the slip-bottom simulation, which means that the along-shelf wavelength of the upstream meander λ increases with time. These are presumably caused by frictional damping that is most effective in the shallower water near the coast. Absence of the bottom friction in the latter case allows persistent acceleration of the along-shelf flow and thus continuous evolution of the lee-wave characteristics. These frictional effects will be discussed in section 5a.

c. Comparison with the CTW model

We now compare the upstream meanders in the slip-bottom ROMS simulations to characteristics of the CTWs resolved by the CTW model to show that the upstream meanders are CTWs generated at the valley and arrested by the shelf flow. For the shelf flow to arrest CTWs, the speed of the eastward shelf flow U_s has to match the westward phase speed of the CTWs c_p, that is, $U_s = -c_p$. In the frequency–wavenumber space, a coastal-trapped lee wave occurs at the intersection between the CTW dispersion curve and the line $\omega = U_s k$ (Brink 1986; Martell and Allen 1979). Here, ω and

$k = 2\pi/\lambda$ are the frequency and wavenumber, respectively. Thus, if the upstream meanders are coastal-trapped lee waves, U_s and λ given by the slip-bottom simulation at any instant time can be used to locate an intersection point in the ω–k space. We use U_s and λ at different times in the slip-bottom ROMS simulation to locate a set of intersection points and construct an empirical CTW dispersion curve.

Along-shelf slices of η' of the slip-bottom upwelling simulation along the center of the anticyclonic flow anomaly at 6-h intervals are used to calculate λ in a way similar to that in the frictional simulations. At the same times, the ambient shelf velocity U_s is obtained from the simulation as the cross-shelf-averaged velocity at $x = -200$ km. The comparison between U_s and λ (pluses in Fig. 13a) shows a positive relationship with an approximately linear trend at $U_s < 0.9$ m s^{-1} and a steeper trend at greater U_s. The initial linear relationship between U_s and λ agrees closely with those obtained from frictional-bottom simulations forced by eastward winds of different strength and also from the simulations of different C_d (Fig. 13a).

The empirical dispersion relation constructed using the U_s and λ series from the slip-bottom simulations (pluses in Fig. 13b) largely matches the mode-2 CTW dispersion curve obtained from the CTW model (green curve in Fig. 13b). In particular, ω experiences a near-linear increase with k at $k < 0.2 \times 10^{-4}$ rad m^{-1}; the dispersion curve flattens around $k = 0.4 \times 10^{-4}$ rad m^{-1} and then transitions to a positive gentle slope at
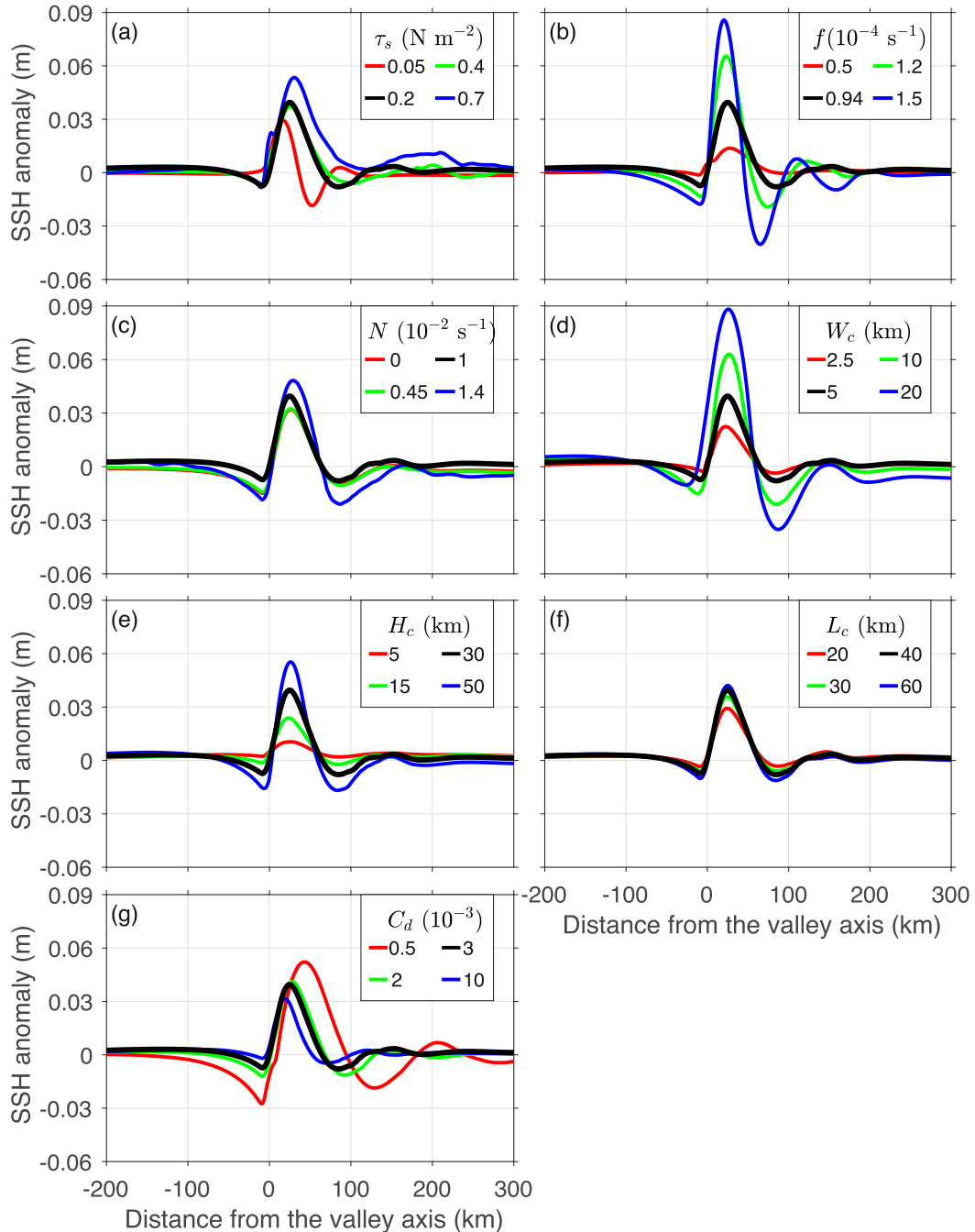
FIG. 10. Along-shelf values of the SSH anomaly at $y = -52$ km (dashed black line in Fig. 3c) at day 5 from upwelling simulations of different (a) wind strength, (b) Coriolis, (c) stratification, (d) valley width, (e) valley depth, (f) valley length, and (g) bottom friction. The black line in each panel is from the upwelling control simulation.

$k > 0.5 \times 10^{-4}$ rad m^{-1} (see below for explanation). Meanwhile, the cross-shelf distributions of the ROMS-simulated η' and U' at day 3 qualitatively match the mode shapes of pressure and along-shelf velocity of the mode-2 CTW resolved by the CTW model, respectively (Figs. 14c,d). These consistencies verify that the

meander to the east of the valley under eastward wind is a coastal-trapped lee wave, that is, a CTW generated at the valley and arrested by the eastward shelf flow. Moreover, the cross-shelf distribution of the initial up-valley flow induced by the valley bathymetry matches the shape of the cross-shelf velocity of the mode-2 CTW
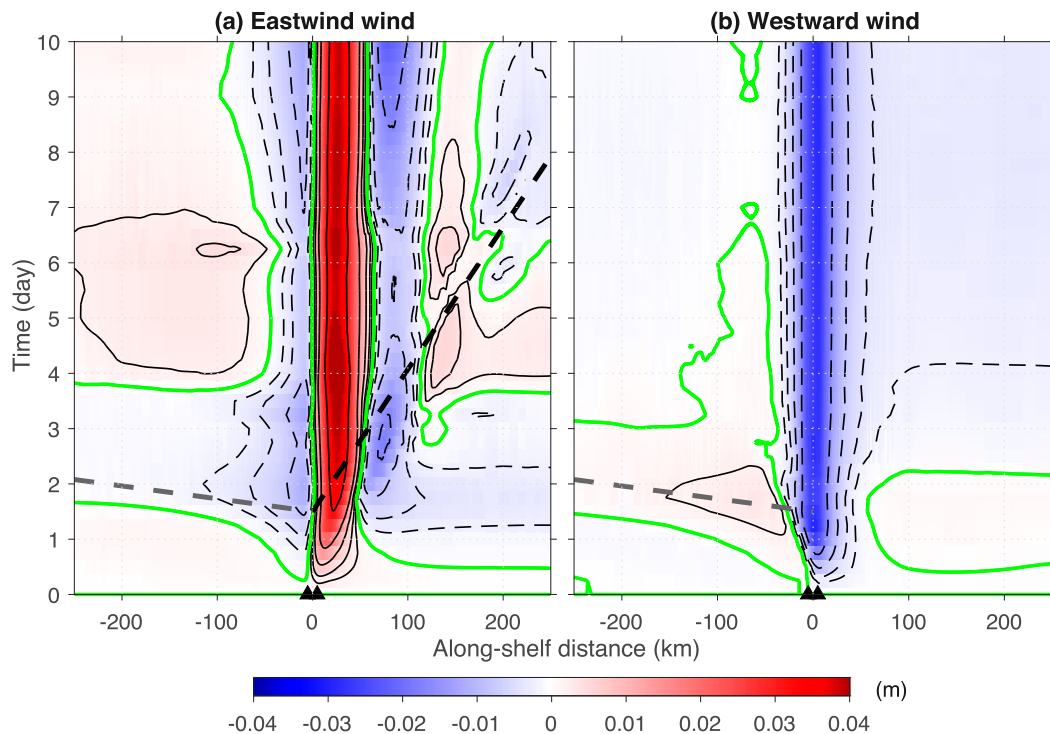
FIG. 11. Hovmöller diagram of the SSH anomaly on the along-shelf section at $y = -52$ km (dashed black line in Fig. 3c) in the cases of (a) eastward and (b) westward wind. The green lines are the contour of zero SSH anomaly; the thin black solid and dashed lines are selected contours of positive and negative SSH anomaly, respectively. The thick black dashed line in (a) indicates the mean speed of the eastward shelf flow, which generally matches the speed of the upstream extension of the SSH anomaly undulation, and thick gray dashed lines in both panels indicate the speed of downstream propagation of mode-1 CTWs, which generally matches the downstream propagation of the initial disturbance generated in the valley. The solid triangles indicate the valley fringe.

(Fig. 14b). These results suggest that the topographically induced initial onshore flow in the valley excites a CTW in the beginning. Trapping of the CTW on the upstream side of the valley then sustains the onshore flow in the valley. Figure 15 shows a schematic plot of the main physical processes and the key links among the parameters. In the downwelling regime, the westward shelf flow allows the initial disturbances induced by the valley bathymetry to propagate freely to the west (Fig. 11b), and the shelf flow then adjusts to bathymetric change and forms a flow pattern symmetric to the valley axis. There are also differences between the empirical dispersion curve and the dispersion curve given by the CTW model (Fig. 13b). They likely result from discrepancies in the model setups, including differences in stratification and cross-shelf profile of the shelf flow. For instance, the CTW model assumes temporally constant stratification, but stratification in the ROMS simulation evolves over time because of mixing and advection (Figs. 4–5). CTW calculations with different stratification give slightly different dispersion curves (Fig. 13b). Moreover, while constructing the empirical dispersion curve, we assume the along-shelf flow is uniform in the cross-shelf direction. The shelf flow in the ROMS model varies in both the vertical and cross-shelf directions (Figs. 4–5), and the associated velocity shear could modify characteristics of the CTWs and also the arresting behavior (Brink 1990; Brooks and Moores 1977).

5. Discussion

a. Mode shape of the arrested CTWs

Comparison between the ROMS and CTW solutions indicates that arrested mode-2 CTWs develop upstream of the valley. In particular, the cross-shelf shape of the upstream meander in the ROMS solution has two zero crossings in U' and one zero crossing in η', consistent with mode-2 CTWs (Figs. 14b,c). There are two likely reasons for mode-2 CTW being arrested here rather than some other CTW mode. First, the lower-mode CTWs are too fast to be arrested by the shelf flow, as indicated by the steep mode-1 CTW dispersion curve (blue line in Fig. 13b). Consistently, the Hovmöller diagrams of η' show very weak initial disturbances
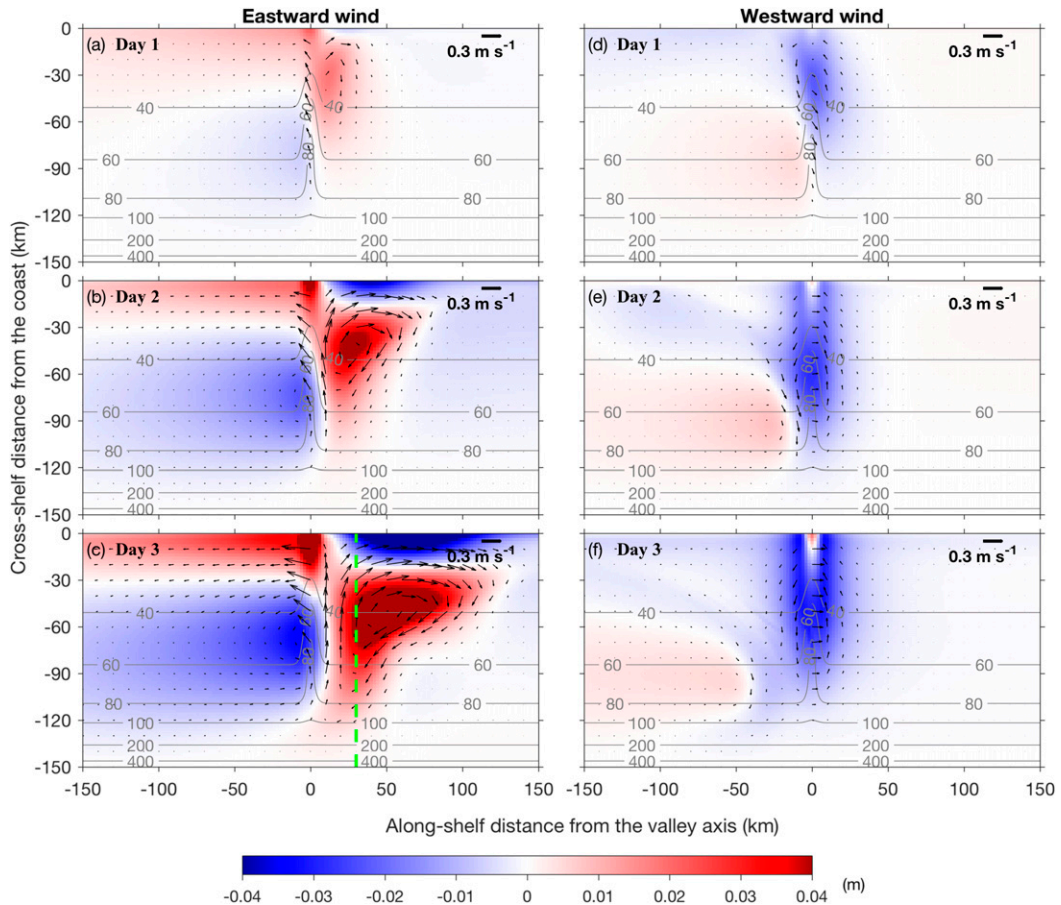
FIG. 12. Time series of SSH anomaly (color) and depth-averaged velocity anomaly (arrows) from the slip-bottom simulations forced by (left) eastward and (right) westward wind. The anomaly is defined as deviation from the conditions at 200 km to the west (east) of the valley in the case of eastward (westward) wind. The gray lines are isobath contours. The dashed green line in (c) indicates the cross section that data in Figs. 14b and 14c are extracted from.

propagating westward at a speed of about $5\,\mathrm{m\,s^{-1}}$ in both upwelling and downwelling regimes (Fig. 11). This signal is consistent with mode-1 CTWs in two aspects: (i) the propagation speed of $5\,\mathrm{m\,s^{-1}}$ is close to the phase speed of the mode-1 CTWs (blue line in Fig. 13b), which is much greater than the shelf flow speed, and (ii) its cross-shelf shape closely resembles the mode shape of the Mode-1 CTW, except in a 5-km-wide region near the coast where the deviation is presumably caused by wind-driven coastal upwelling (Figs. 14g,h).

Second, the initial up-valley flow inside the valley has its maximum at the midshelf, and the associated cross-shelf shape fits the structure of mode-2 CTW better than the structure of CTWs of other modes (Fig. 14b). The initial up-valley flow thus excites mode-2 CTW the most effectively (Martell and Allen 1979). Consistently, the amplitude of the rapidly propagating mode-1 waves is about 40 times weaker than the mode-2 waves (Figs. 14g,h).

The peak of the initial up-valley flow is located at mid-shelf because the onshore pressure gradient force is the strongest at midshelf where the valley bathymetric deviation from the ambient shelf is the greatest. These cause mode-2 CTWs to dominate the waves generated and arrested at the valley. That is, the dominant mode of the CTW to be arrested is the one whose cross-shelf modal structure fits the best onto the cross-shelf bathymetric perturbation of the valley, an argument similar to that in Brink (1986). The partition of the energy among the different modes generated at the valley remains a question to be investigated.

b. Effect of the bottom friction

To examine the influence of bottom friction, we construct an empirical ω–k relation using U_s and λ from the upwelling ROMS simulations with bottom friction forced by eastward winds of different strength (triangles
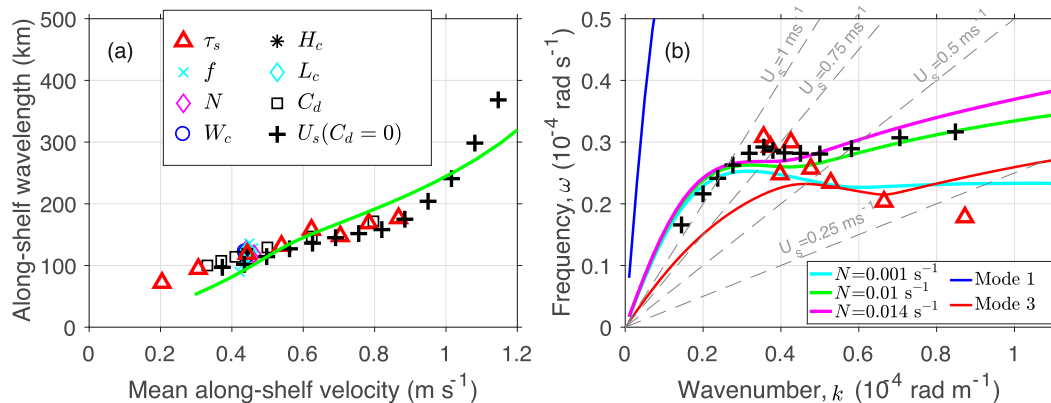
FIG. 13. (a) Variation of the along-shelf wavelength with respect to the cross-shelf-averaged along-shelf velocity from all sensitivity simulations; (b) the dispersion curves obtained from the CTW model with different upper-layer stratification (colored solid lines) and the empirical dispersion relation given by simulations with (red triangles) and without (black pluses) bottom friction. Each type of symbol in (a) represents results from a set of sensitivity simulations that vary a parameter corresponding to the legend. Results of the simulations varying f, N, W_c, H_c, and L_c are all clustered around $U_s = 0.45 \, \mathrm{m \, s^{-1}}$ and $\lambda = 120 \, \mathrm{km}$. The green line in (a) represents the theoretical wavelength flow curve obtained from the CTW dispersion curve with the upper-layer stratification of $N = 0.01 \, \mathrm{s^{-1}}$. The blue and red line in (b) represents the mode-1 and mode-3 CTW dispersion curves estimated using the CTW model, respectively. The dashed gray lines in (b) are examples of the line $\omega = U_s k$ intersecting the mode-2 CTW dispersion curve.

in Fig. 13b). The ambient along-shelf flow in these simulations increases with the wind stress, which causes η' and λ to increase (Fig. 10a), a pattern similar to that in the ROMS simulations with a slip bottom.

However, the empirical ω–k relation obtained from the frictional-bottom simulations is quite different from that of the slip-bottom simulation. First, the dispersion relation from the frictional-bottom simulations misses the positive ω–k relationship in the low k regime because the bottom friction suppresses the along-shelf flow. With wind stress of $0.7 \, \mathrm{N \, m^{-2}}$, the upper bound of wind stress in the HSV region (Lentz et al. 2014), the modeled U_s is less than $0.9 \, \mathrm{m \, s^{-1}}$, and λ is about $175 \, \mathrm{km}$ (Figs. 10a, 13a). Both are substantially less than the high values achieved in the slip-bottom simulation. Second, with bottom friction, ω decreases with increasing k at high k, a trend opposite to the slip-bottom result (Fig. 13b). Presumably, this is caused by the damping effect of the bottom friction (Brink 2006). The exact mechanism of bottom friction affecting the short coastal-trapped lee waves is unknown and left for future studies. Interestingly, cross-shelf distribution of initial up-valley flow and η' in slip- and frictional-bottom simulations are similar, while U' near the coast is strongly damped by the bottom friction (Fig. 14). This effect of the bottom friction is consistent with the findings of previous studies (e.g., Brink 2006; Power et al. 1989) that bottom friction moves the maximum flow associated with CTWs offshore while maintaining the wave pressure field over the shelf.

c. Sensitivity to model parameters

We now examine the dependence of lee-wave characteristics on variations in τ_s, W_c, L_c, H_c, f, C_d, and N in the different upwelling simulations. For each of the sensitivity simulation, the SSH anomaly η' is estimated with respect to SSH at $x = -200 \, \mathrm{km}$ at day 5 and at the along-shelf slice at $y = -52 \, \mathrm{km}$ (Fig. 10).

All simulations show qualitatively similar along-shelf patterns of η' with large-amplitude undulations occurring to the east of the valley. This indicates that the basic mechanism of the shelf flow arresting CTWs and forming a lee wave on the upstream side of the valley applies to shelf valleys within the parameter range examined here. However, the amplitude of the undulation varies among the simulations. For instance, the maximum η' increases dramatically with f, W_c, and H_c. This means that the up-valley velocity is sensitive to these parameters, as the undulation amplitude is connected to the up-valley velocity through the geostrophic balance in the cross-valley direction. The parameter dependence of the up-valley velocity is examined in Part II.

The lee-wave wavelength λ increases with increasing τ_s, decreasing C_d, and, to a lesser extent, with decreasing f and N. The wavelength λ does not vary with W_c, L_c, and H_c (Figs. 10d–f, 13a). These relationships are all consistent with the upstream meanders being coastal-trapped lee waves. As described in section 4, λ is determined by where the CTW dispersion curve intersects the line of $\omega = U_s k$ in the ω–k space. Given the
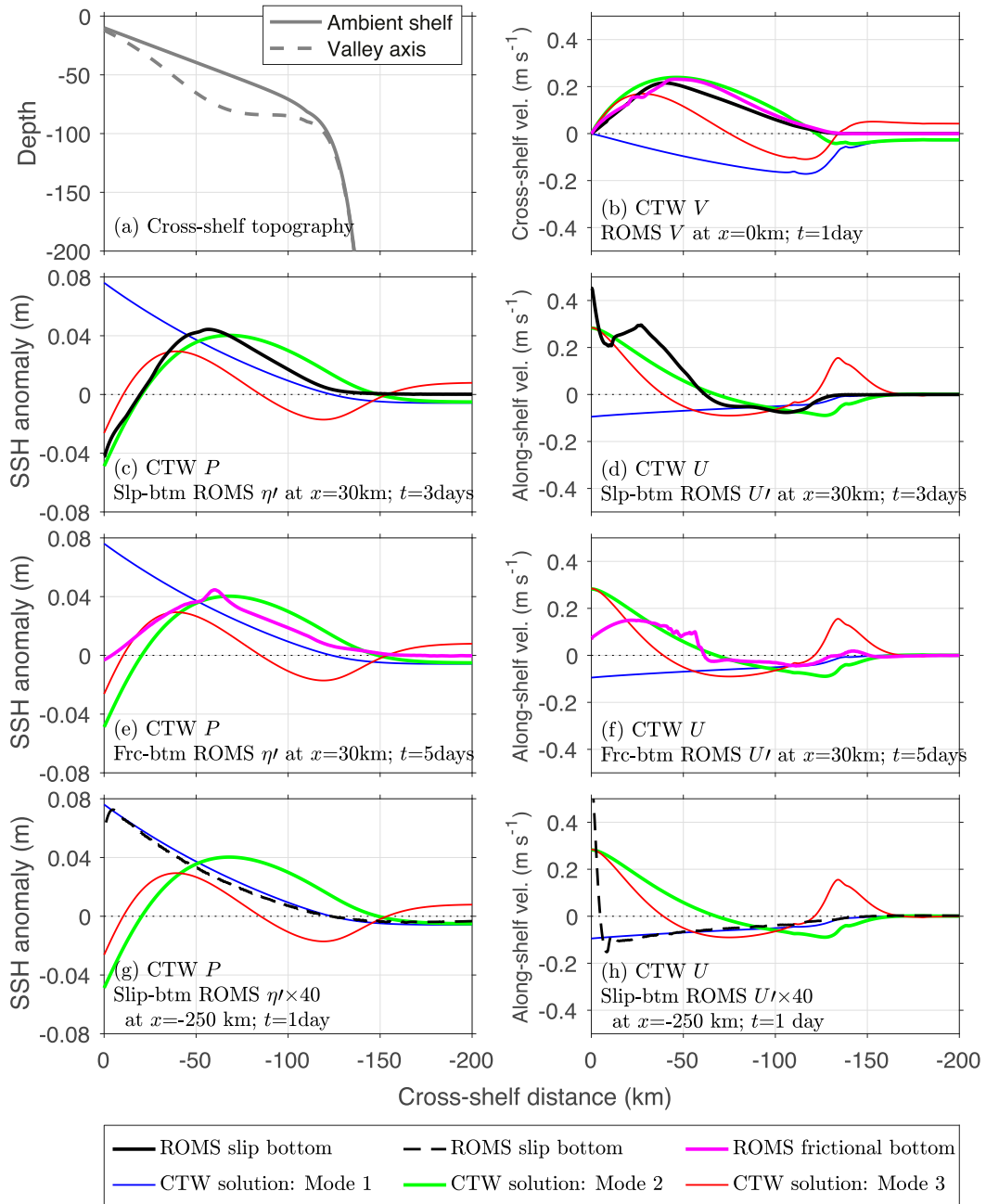
FIG. 14. (a) Cross-shelf bathymetry in the valley and on the ambient shelf; cross-shelf structure of (b) V, (c),(e), (g) P (or equivalently η'), and (d),(f),(h) U given by both the CTW model and the upwelling ROMS simulations with, in (c), (d) (g), and (h), and without, in (e) and (f), bottom friction. The ROMS results in (c) and (d) are obtained at $x = 30$ km (green dashed line in Fig. 12c) and $t = 3$ days; those in (e) and (f) are at $x = 30$ km (green dashed line in Fig. 3c) and $t = 5$ days. Note that the CTW solutions in the lower three rows are the same. The ROMS η' and U' in (g) and (h) are multiplied by 40 to put them on the same scale as the other panels, and they are obtained at $x = -250$ km and $t = 1$ day relative to $x = -450$ km at the same time, corresponding to the signal propagating rapidly downstream during the initial adjustment period (gray dashed line in Fig. 11a). The ROMS V in (b) is obtained at $x = 0$ km and $t = 1$ day, depicting the topographically driven initial disturbance that excites CTWs.
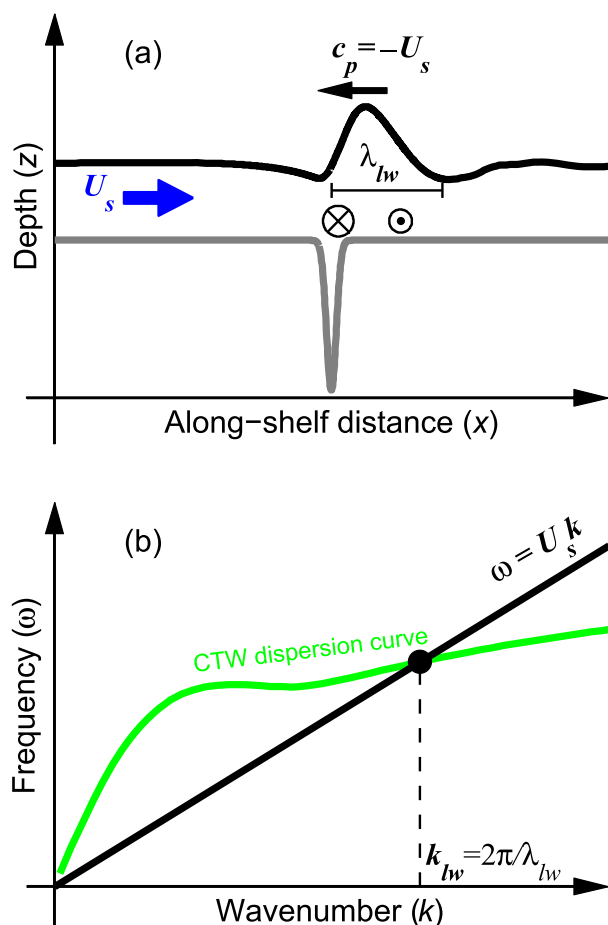
FIG. 15. A schematic summarizing the key elements: (a) the shelf current U_s arresting a CTW that has a phase velocity c_p opposite to the shelf flow velocity and the resulting lee wave (lw; black line) on the upstream side of the valley; (b) the coastal-trapped lee wave is located at the intersection between the CTW dispersion curve and the $\omega = U_s k$ line in the ω–k space, and the wavelength of the coastal-trapped lee wave corresponds to the wavenumber at the intersection. The gray line in (a) is bathymetry.

quantify this remote influence through establishing the connection between the upstream flow variability and the flow forcing. For instance, if the mean shelf current is weak relative to the wind-induced shelf flow, the valley-induced upstream variability would be correlated with the wind fluctuations and could be investigated in the field. If the shelf flow is driven by some persistent forcing, such as the onshore impingement of a large offshore eddy with a flow that opposes the CTW phase propagation, a persistent upstream meander influence would be expected and can be observationally quantified.

d. Relevance to slope canyons

The basic mechanism of generating coastal-trapped lee waves and sustaining an onshore current by an ambient along-isobath flow opposing CTW phase propagation is expected to be applicable to deeper slope canyons incising the offshore edges of continental shelves. The key ingredients for generating coastal-trapped lee waves are CTWs, an along-isobath flow in the opposite direction to the CTW phase propagation, and a bathymetric perturbation that generates an initial onshore flow. Changing the geometry of the bathymetric perturbation from a shallow valley to a deep canyon and moving it offshore to the shelf edge do not fundamentally change the initial onshore flow or the CTW propagation. This explains the qualitative similarities between the asymmetrical flow responses in shelf valleys and in slope canyons. Note that most of the slope canyon studies impose ambient flows, rather than using winds to generate the flow. Other processes, including large-scale open-ocean forcing, for example, impinging warm-core rings (Zhang and Gawarkiewicz 2015), could also generate the needed ambient along-slope current. Differences in the generation mechanism of the ambient along-isobath flow are unlikely to affect the formation of coastal-trapped lee waves.

The exact shape of the coastal-trapped lee waves, as determined by the cross-shelf mode, and the extent of the upstream influence may vary with the cross-shelf location and geometry of the bathymetric perturbation. For instance, we speculate that, for a slope canyon at the edge of a wide continental shelf (e.g., the Mid-Atlantic Bight), the initial onshore flow generated by the bathymetric perturbation will concentrate at the shelf edge. This cross-shelf pattern may fit better the shape of CTW of a higher mode and excite CTWs of that mode more effectively. For the same ambient along-shelf flow as presented in this study, the intersection between the CTW dispersion curve and the $\omega = U_s k$ line would occur at lower wavenumber if everything else remains the same, as the dispersion curve shifts toward lower frequency with increasing

ambient shelf bathymetry and stratification, the CTW dispersion curve steepens with increasing f or N, which causes the intersection to move slightly toward a higher wavenumber when U_s is fixed. For a given f, the intersection moves toward a lower wavenumber when U_s increases as a result of increasing τ_s or decreasing C_d. Changing the valley geometry does not change U_s or the CTW dispersion relation and thus has no effect on λ.

The persistent flow meander upstream of the shelf valley has important implications for studies of flow variability on continental shelves. It means that irregular shelf bathymetry can not only affect local flow but also induce significant flow variability 10–100 km away. Because the spatial extent and intensity of the upstream influence are sensitive to the shelf flow, it is feasible to

mode number. Consequently, the flow variability induced by the canyon may reach farther upstream.

Additionally, the increased vertical scale in the slope canyons might allow the stratification to play a more important role in the CTW dynamics. As S in slope canyons are generally greater than those in this study, canyon flows are likely more sensitive to stratification. All these considerations call for specifically designed numerical or observational studies to understand the characteristics of coastal-trapped lee waves at slope canyons and the influence of the canyons on the shelf and slope currents.

6. Summary

This study investigates wind-driven flows in idealized shelf valleys that mimic the geometry of HSV. The main motivation is the observed, wind-driven up-valley flow in HSV is much stronger than the wind-driven down-valley flow even with similar strength of the surface wind stress. This first part of the two-part sequence focuses on the mechanism of the asymmetrical response of the valley flow to along-shelf winds of opposite directions. ROMS model simulations (Fig. 2) show that when the wind is in the same direction as CTW phase propagation, the along-shelf flow tends to roughly follow the isobaths and forms an onshore detour pattern over the valley with very weak net down-valley transport. When the wind is in the opposite direction to CTW propagation, persistent onshore flow with strong up-valley transport occurs in the valley and a stationary meandering flow pattern develops on the upstream side of the valley (in the sense of CTW propagation). This asymmetry in the wind-driven valley flows was present in all the simulations with a shelf-slope bathymetry. It also resembles the asymmetrical flow response in slope canyons driven by along-slope currents of opposite directions (e.g., Allen and Durrieu de Madron 2009; Allen and Hickey 2010; Kämpf 2006, 2009; Klinck 1996; She and Klinck 2000).

This study shows that the asymmetry is caused by a coastal-trapped lee wave that develops upstream (CTW sense) of the valley when the wind-driven along-shelf flow opposes CTW phase propagation (i.e., the upwelling regime). That is, the bathymetric perturbation drives an initial up-valley flow and induces CTWs; the wind-driven shelf flow arrests the CTW having the phase velocity opposite to the shelf velocity and the arrested CTW sustains the onshore flow in the valley (Fig. 15). In contrast, when the shelf flow is in the same direction as CTW phase propagation (i.e., the downwelling regime), the bathymetrically generated initial flow disturbances propagate away from the valley, and there is no lee wave. In support of this idea, the wavelength of the upstream meander in all the upwelling regime model simulations is reproduced by lee-wave wavelength estimates based on the along-shelf current and dispersion relationship for CTWs from a linear, inviscid CTW model (Fig. 13). The cross-shelf sea level and current variations in the upstream meander are consistent with the cross-shelf modal structure of the predicted lee wave (Fig. 14).

Sensitivity simulations show that the amplitude of the arrested CTWs under eastward winds and the up-valley flow vary with wind stress, Coriolis, stratification, valley geometry, and bottom friction. The details of the relationships are investigated in Part II. Meanwhile, the wavelength of the meander varies with only the parameters that affect the intersection in the frequency–wavenumber space between the CTW dispersion curve and the straight line with a slope of the shelf flow speed, that is, wind stress, Coriolis, stratification, and bottom friction. The meander wavelength is independent of the valley geometrical parameters that do not affect the shelf flow or the CTW characteristics.

The fundamental mechanism of shelf flow arresting CTWs and causing asymmetrical valley flow response to along-shelf flows of opposite directions is expected to be applicable to other shelf and slope bathymetric features, such as slope canyons. However, details of the induced cross-isobath flows would depend on various factors, including shelf and slope bathymetry, Coriolis, stratification, as well as the canyon bathymetry. The findings of this study also imply that irregular bathymetric features on a continental shelf can induce flow variation over a region that is much larger than the bathymetric feature. Understanding variability of flows on a continental shelf would thus require taking bathymetric features over a wide region into consideration.

REFERENCES

Allen, S. E., and X. Durrieu de Madron, 2009: A review of the role of submarine canyons in deep-ocean exchange with the shelf. *Ocean Sci.*, **5**, 607–620, https://doi.org/10.5194/os-5-607-2009.

——, and B. M. Hickey, 2010: Dynamics of advection-driven upwelling over a shelf break submarine canyon. *J. Geophys. Res.*, **115**, C08018, https://doi.org/10.1029/2009JC00573.

Bosley, K. L., J. W. Lavelle, R. D. Brodeur, W. W. Wakefield, R. L. Emmett, E. T. Baker, and K. M. Rehmke, 2004: Biological and physical processes in and around Astoria submarine canyon, Oregon, USA. *J. Mar. Syst.*, **50**, 21–37, https://doi.org/10.1016/j.jmarsys.2003.06.006.

Boyer, D. L., D. B. Haidvogel, and N. Perenne, 2004: Laboratory–numerical model comparisons of canyon flows: A parameter study. *J. Phys. Oceanogr.*, **34**, 1588–1609, https://doi.org/10.1175/1520-0485(2004)034<1588:LMCOCF>2.0.CO;2.

——, J. Sommeria, A. S. Mitrovic, V. K. C. Pakala, S. A. Smirnov, and D. Etling, 2006: The effects of boundary turbulence on canyon flows forced by periodic along-shelf currents. *J. Phys. Oceanogr.*, **36**, 813–826, https://doi.org/10.1175/JPO2866.1.

Brink, K. H., 1986: Topographic drag due to barotropic flow over the continental shelf and slope. *J. Phys. Oceanogr.*, **16**, 2150–2158, https://doi.org/10.1175/1520-0485(1986)016<2150:TDDTBF>2.0.CO;2.

——, 1990: On the damping of free coastal-trapped waves. *J. Phys. Oceanogr.*, **20**, 1219–1225, https://doi.org/10.1175/1520-0485(1990)020<1219:OTDOFC>2.0.CO;2.

——, 2006: Coastal-trapped waves with finite bottom friction. *Dyn. Atmos. Oceans*, **41**, 172–190, https://doi.org/10.1016/j.dynatmoce.2006.05.001.

Brooks, D. A., and C. N. K. Moores, 1977: Free, stable continental shelf waves in a sheared barotropic boundary current. *J. Phys. Oceanogr.*, **7**, 380–388, https://doi.org/10.1175/1520-0485(1977)007<0380:FSCSWI>2.0.CO;2.

Chapman, D. C., 1985: Numerical treatment of cross-shelf open boundaries in a barotropic ocean model. *J. Phys. Oceanogr.*, **15**, 1060–1075, https://doi.org/10.1175/1520-0485(1985)015<1060:NTOCSO>2.0.CO;2.

Connolly, T. P., and B. M. Hickey, 2014: Regional impact of submarine canyons during seasonal upwelling. *J. Geophys. Res. Oceans*, **119**, 953–975, https://doi.org/10.1002/2013JC009452.

Crockett, J. C., C. A. Nittrouer, A. S. Ogston, D. F. Naar, and T. T. Donahue, 2008: Morphology and filling of incised submarine valleys on the continental shelf near the mouth of the Fly River, Gulf of Papua. *J. Geophys. Res.*, **113**, F01S12, https://doi.org/10.1029/2006JF000674.

Flather, R. A., 1976: A tidal model of the northwest European continental shelf. *Mem. Soc. Roy. Sci. Liege*, **10**, 141–164.

Freeland, H. J., and K. L. Denman, 1982: A topographically controlled upwelling center off southern Vancouver Island. *J. Mar. Res.*, **40**, 1069–1093.

Haidvogel, D. B., 2005: Cross-shelf exchange driven by oscillatory barotropic currents at an idealized coastal canyon. *J. Phys. Oceanogr.*, **35**, 1054–1067, https://doi.org/10.1175/JPO2735.1.

Harris, C. K., B. Butman, and P. Traykovski, 2003: Winter-time circulation and sediment transport in the Hudson shelf valley. *Cont. Shelf Res.*, **23**, 801–820, https://doi.org/10.1016/S0278-4343(03)00025-6.

Harris, P. T., and T. Whiteway, 2011: Global distribution of large submarine canyons: Geomorphic differences between active and passive continental margins. *Mar. Geol.*, **285**, 69–86, https://doi.org/10.1016/j.margeo.2011.05.008.

Haynes, P. H., E. R. Johnson, and R. G. Hurst, 1993: A simple model of Rossby-wave hydraulic behaviour. *J. Fluid Mech.*, **253**, 359–384, https://doi.org/10.1017/S0022112093001831.

Hickey, B. M., 1997: The response of a steep-sided, narrow canyon to time-variable wind forcing. *J. Phys. Oceanogr.*, **27**, 697–726, https://doi.org/10.1175/1520-0485(1997)027<0697:TROASS>2.0.CO;2.

——, E. Baker, and N. Kachel, 1986: Suspended particle movement in and around Quinault submarine canyon. *Mar. Geol.*, **71**, 35–83, https://doi.org/10.1016/0025-3227(86)90032-0.

Johnson, E. R., and S. R. Clarke, 1999: Dispersive effects in Rossby-wave hydraulics. *J. Fluid Mech.*, **401**, 27–54, https://doi.org/10.1017/S0022112099006849.

——, and ——, 2001: Rossby wave hydraulics. *Annu. Rev. Fluid Mech.*, **33**, 207–230, https://doi.org/10.1146/annurev.fluid.33.1.207.

Kämpf, J., 2006: Transient wind-driven upwelling in a submarine canyon: A process-oriented modeling study. *J. Geophys. Res.*, **111**, C11011, https://doi.org/10.1029/2006JC003497.

——, 2009: On the interaction of time-variable flows with a shelf-break canyon. *J. Phys. Oceanogr.*, **39**, 248–260, https://doi.org/10.1175/2008JPO3753.1.

——, 2012: Lee effects of localized upwelling in a shelf-break canyon. *Cont. Shelf Res.*, **42**, 78–88, https://doi.org/10.1016/j.csr.2012.05.005.

Killworth, P. D., 1978: Coastal upwelling and Kelvin waves with small longshore topography. *J. Phys. Oceanogr.*, **8**, 188–205, https://doi.org/10.1175/1520-0485(1978)008<0188:CUAKWW>2.0.CO;2.

Klinck, J. M., 1989: Geostrophic adjustment over submarine canyons. *J. Geophys. Res.*, **94**, 6133–6144, https://doi.org/10.1029/JC094iC05p06133.

——, 1996: Circulation near submarine canyons: A modeling study. *J. Geophys. Res.*, **101**, 1211–1223, https://doi.org/10.1029/95JC02901.

Lentz, S. J., B. Butman, and C. Harris, 2014: The vertical structure of the circulation and dynamics in Hudson shelf valley. *J. Geophys. Res. Oceans*, **119**, 3694–3713, https://doi.org/10.1002/2014JC009883.

Liu, Z., and J. Gan, 2015: Upwelling induced by the frictional stress curl and vertical squeezing of the vortex tube over a submerged valley in the East China Sea. *J. Geophys. Res. Oceans*, **120**, 2571–2587, https://doi.org/10.1002/2015JC010715.

Manning, J. P., L. Y. Oey, D. Packer, J. Vitaliano, T. W. Finneran, K. W. You, and S. Fromm, 1994: Observations of bottom currents and estimates of resuspended sediment transport at the New York Bight 12-mile dumpsite. *J. Geophys. Res.*, **99**, 10 221–10 239, https://doi.org/10.1029/93JC03273.

Martell, C. M., and J. S. Allen, 1979: The generation of continental shelf waves by alongshore variations in bottom topography. *J. Phys. Oceanogr.*, **9**, 696–711, https://doi.org/10.1175/1520-0485(1979)009<0696:TGOCSW>2.0.CO;2.

Michels, K. H., A. Suckow, M. Breitzke, H. R. Kudrass, and B. Kottke, 2003: Sediment transport in the shelf canyon "Swatch of No Ground" (Bay of Bengal). *Deep-Sea Res. II*, **50**, 1003–1022, https://doi.org/10.1016/S0967-0645(02)00617-3.

Narimousa, S., and T. Maxworthy, 1985: Two-layer model of shear-driven coastal upwelling in the presence of bottom topography. *J. Fluid Mech.*, **159**, 503–531, https://doi.org/10.1017/S0022112085003329.

Power, S. B., J. H. Middleton, and R. H. J. Grimshaw, 1989: Frictionally modified continental shelf waves and the subinertial response to wind and deep-ocean forcing. *J. Phys. Oceanogr.*, **19**, 1486–1506, https://doi.org/10.1175/1520-0485(1989)019<1486:FMCSWA>2.0.CO;2.

Schiller, R. V., V. H. Kourafalou, P. Hogan, and N. D. Walker, 2011: The dynamics of the Mississippi River plume: Impact of topography, wind and offshore forcing on the fate of plume waters. *J. Geophys. Res.*, **116**, C06029, https://doi.org/10.1029/2010JC006883.

Shchepetkin, A. F., and J. C. McWilliams, 2008: Computational kernel algorithms for fine-scale, multiprocess, long-term oceanic simulations. *Handbook of Numerical Analysis. XIV: Computational Methods for the Atmosphere and the Ocean*, P. G. Ciarlet, R. Temam, and J. Tribbia, Eds., Elsevier, 121–183.

She, J., and J. M. Klinck, 2000: Flow near submarine canyons driven by constant winds. *J. Geophys. Res.*, **105**, 28 671–28 694, https://doi.org/10.1029/2000JC900126.

Wang, D.-P., and C. N. K. Mooers, 1976: Coastal-trapped waves in a continuously stratified ocean. *J. Phys. Oceanogr.*, **6**, 853–863, https://doi.org/10.1175/1520-0485(1976)006<0853:CTWIAC>2.0.CO;2.

Williams, W. J., E. C. Carmack, K. Shimada, H. Melling, K. Aagaard, R. W. Macdonald, and R. G. Ingram, 2006: Joint effects of wind and ice motion in forcing upwelling in Mackenzie Trough, Beaufort Sea. *Cont. Shelf Res.*, **26**, 2352–2366, https://doi.org/10.1016/j.csr.2006.06.012.

Yankovsky, A. E., and D. C. Chapman, 1997: Anticyclonic eddies trapped on the continental shelf by topographic irregularities.

J. Geophys. Res., **102**, 5625–5639, https://doi.org/10.1029/96JC03452.

Zhang, W. G., and G. G. Gawarkiewicz, 2015: Dynamics of the direct intrusion of Gulf Stream ring water onto the Mid-Atlantic Bight shelf. *Geophys. Res. Lett.*, **42**, 7687–7695, https://doi.org/10.1002/2015GL065530.

——, J. L. Wilkin, and R. J. Chant, 2009: Modeling the pathways and mean dynamics of river plume dispersal in New York Bight. *J. Phys. Oceanogr.*, **39**, 1167–1183, https://doi.org/10.1175/2008JPO4082.1.